J. Fluid Mech. (1991), vol. 225, pp. 121–152
Printed in Great Britain

Granular flow: physical experiments and their implications for microstructural theories

By THOMAS G. DRAKE†

Department of Earth and Space Sciences, University of California, Los Angeles, CA 90024-1567, USA

(Received 23 March 1990 and in revised form 28 August 1990)

Positions, velocities and rotations of individual particles obtained from high-speed motion pictures of essentially two-dimensional flows of plastic spheres in an inclined glass-walled chute were used to test critical assumptions of microstructural theories for the flow of granular materials. The measurements provide a well-defined set of observations for refining and validating computer simulations of granular flows, and point out some important limitations of physical experiments. Two nearly steady, uniform, collisional flows of 6-mm-diameter plastic spheres over a fixed bed of similar spheres inclined at 42.75° were analysed in detail. Particle fluxes were about 2230 particles s^{-1} and 1280 particles s^{-1}. The nominal depth in both flows was about 18 particle diameters. Profiles of mean downstream velocity and mean rotations, translational temperature and rotational temperature, and bulk density in the flows show slip at the bed of 17 and 26% of the mean flow velocity for the high- and low-flux flows, respectively; mean rotation rates $\bar{\omega}_x$ and $\bar{\omega}_y$ less than 9% of $\bar{\omega}_z$ ($\hat{\boldsymbol{e}}_x$ parallel to the bed, $\hat{\boldsymbol{e}}_z$ normal to the sidewall); translational temperature nearly independent of distance from the bed; rotational temperature decreasing with distance from the bed; and density decreasing almost linearly with distance from the bed. The continuum hypothesis (i.e. small gradients in mean-flow properties) is satisfied throughout the flow except near the fixed bed, where large gradients in the mean rotation $\bar{\omega}_z$ and downstream velocity occur over a few particle diameters. The distributions of velocities and rotations are approximately Maxwellian, except near the fixed bed. Testing microstructural theories with physical experiments is severely hampered by limitations on material properties of particles, flow lengthscale and the spatial and temporal resolution of observations. Only a small volume of the parameter space for collision-dominated flows can reasonably be explored by physical experiment. Extraneous forces due to air drag, sidewall friction and electrical effects are not included in theories but must be addressed in physical experiments. Properly designed experiments are the essential link between computer simulations and theory, because they focus attention on particular features critical to testing the simulations, which in turn provide detailed particle-scale information needed to test theories.

1. Introduction

The modification of the kinetic theory for dense gases to describe collision-dominated flows of granular material represents a paradigm change that has greatly advanced understanding of granular flows. Direct particle-scale observations from

† Present address: Center for Coastal Studies, Scripps Institution of Oceanography, University of California, La Jolla, CA, 92093-0209, USA.

physical experiments have played little role in the formulation of these theories, however, largely because of the difficulties in observing particle motions in the interiors of granular flows without disturbing them. Thus, despite the microstructural nature of the new theories, their development has been driven primarily by bulk-flow observations of granular flows, physical experiments yielding such macroscopic quantities as the stresses exerted on the boundaries of viscometric devices, and computer simulations. This paper presents measurements of velocities and rotations of individual spherical particles in essentially two-dimensional flows in an inclined glass-walled chute. The results test critical theoretical assumptions, provide a well-defined set of observations for refining and validating computer simulations, and point out some important limitations of physical experiments.

Momentum exchange in *grain flows* arises primarily from direct particle-to-particle contact, and any momentum exchange derived from the influence of interstitial fluids, if present, is negligible. Two end-member flow regimes are recognized in grain flows: the *collisional* regime, in which momentum is dominated by well-defined collisions between particles, and the *frictional* regime, in which it is dominated by persistent rubbing of particles against their neighbours. Both collisional and frictional effects are important in many chute flows; however, microstructural theories based on analogies to the kinetic theory of gases (e.g. Haff 1983; Jenkins & Savage 1983; Savage 1983; Lun *et al.* 1984; Jenkins & Richman 1985*a*, *b*; Araki & Tremaine 1986; Lun & Savage 1987; Gutt 1987; Gutt & Haff 1988) have been applied only to collisional flows. This paper focuses on observations of particle motion in disperse, nearly structureless, collisional grain flows to which such kinetic theories might be applied. Drake (1990) describes structural features from a particle-scale perspective in a variety of collisional and frictional grain flows of identical spheres in an inclined glass-walled chute.

1.1. *Kinetic theory assumptions*

The following section outlines the critical features and assumptions of the continuum kinetic theories, placing emphasis on those aspects of the theoretical formulations that may be challenged experimentally: the continuum hypothesis, velocity distribution functions, collision models and boundary conditions.

The ensemble average of some scalar or vector property ψ (e.g. the velocity) associated with individual particles is defined as

$$\langle \psi \rangle = \frac{1}{n} \int \psi f^{(1)}(\boldsymbol{c}, \boldsymbol{r}) \, \mathrm{d}\boldsymbol{c} \tag{1}$$

where $f^{(1)}$ is a single-particle velocity distribution function defined such that $f^{(1)} \, \mathrm{d}\boldsymbol{c}$ is the differential number of particles contained in the volume element $\mathrm{d}\boldsymbol{r}$ having velocities in the range $\boldsymbol{c}$ to $\boldsymbol{c} + \mathrm{d}\boldsymbol{c}$, and $n = n(\boldsymbol{r})$ is the number density of particles. To ensure the validity of the continuum hypothesis, the volume element $\mathrm{d}\boldsymbol{r}$ must simultaneously satisfy the requirements that it contain enough particles that ψ, $f^{(1)}$, and n are statistically meaningful, yet be sufficiently small that changes of these quantities across it are negligible. From the viewpoint of the experimentalist, testing the continuum hypothesis implicitly assumes that the relevant statistical averaging can be accomplished. Because the particles and their spacing are much larger relative to the scale of the flow than in ordinary gases, deducing such bulk properties as mean velocity $\langle \boldsymbol{u} \rangle$ or granular temperature $T_{\mathrm{r}} = \frac{1}{2}(\langle u'^2 \rangle + \langle v'^2 \rangle)$ necessitates analysis of observations on many individual particles, i.e. there is no convenient granular analog

for the common thermometer. Thus, a direct conflict arises between describing fluctuations in particle properties in small volumes over short times, and the concomitant need to determine global flow properties such as flow steadiness and uniformity, which requires more synoptic measurements.

The single-particle distribution function $f^{(1)}$ is typically assumed to be Maxwellian:

$$f^{(1)}(\boldsymbol{c},\boldsymbol{r}) = n(2\pi T)^{-\frac{3}{2}}\exp\left[\frac{-(c-u)^2}{2T}\right]. \tag{2}$$

The probability of any given collision between two particles is described by the complete collisional pair distribution function $f^{(2)}$, which is the product of a pair distribution function $g(\boldsymbol{r}_1,\boldsymbol{r}_2)$ and the single-particle velocity distribution functions for each particle:

$$f^{(2)}(\boldsymbol{c}_1,\boldsymbol{r}_1,\boldsymbol{c}_2,\boldsymbol{r}_2) = g(\boldsymbol{r}_1,\boldsymbol{r}_2)f^{(1)}(\boldsymbol{c}_1,\boldsymbol{r}_1)f^{(1)}(\boldsymbol{c}_2,\boldsymbol{r}_2), \tag{3}$$

where $\boldsymbol{r}$ is the position and the subscripts 1 and 2 identify the particles. The statistics of the spatial arrangement of pairs of particles is given by $g(\boldsymbol{r}_1,\boldsymbol{r}_2)$. In a shearing granular flow, the distribution of collisions will not be homogeneous, and g will, in general, be a function of $\boldsymbol{u}_1$, $\boldsymbol{u}_2$ and T, as well as $|\boldsymbol{r}_1-\boldsymbol{r}_2|$. Jenkins & Savage (1983) used dimensional arguments to arrive at a general form for g that was linear in the rate of shear, based on the assumption that $|\sigma\nabla\boldsymbol{u}|\,T^{-\frac{1}{2}} \ll 1$, where σ is the particle diameter. Although other workers have avoided this restriction by including higher-order terms, the resulting theories can treat only frictionless particles and would be extremely difficult to extend further (Lun *et al.* 1984, p. 245). As a consequence, the assumption of small gradients in mean-flow properties is likely to be critical in theories that can be tested with physical experiments.

Implicit in the formulation of $f^{(2)}$ as the product of two single-particle velocity distribution functions is the assumption of molecular chaos or statistical independence of the particle velocities, which is clearly violated in typical granular flows. Finally, none of the kinetic theories for granular flow treat simultaneous collisions of three or more particles. While binary collisions predominate in the disperse flows described in this paper, many granular flows are at least partially frictional (Drake 1990), in which case the binary-collision hypothesis is inappropriate.

Evaluating constitutive integrals in the kinetic theories requires simple collision models which describe post-collision particle trajectories in terms of pre-collision ones. Early theories accounted only for the translational energy lost in collisions through a constant normal coefficient of restitution ϵ:

$$\boldsymbol{k}\cdot\tilde{\boldsymbol{u}}_{12} = -\epsilon(\boldsymbol{k}\cdot\boldsymbol{u}_{12}). \tag{4}$$

Here $\boldsymbol{k}$ is the unit vector directed from the centre of particle 1 to the centre of particle 2, and $\boldsymbol{u}_{12} = \boldsymbol{u}_1-\boldsymbol{u}_2$ and $\tilde{\boldsymbol{u}}_{12} = \tilde{\boldsymbol{u}}_1-\tilde{\boldsymbol{u}}_2$ are the total relative velocities of the particles at the point of contact just before and after collision.

Surface friction also dissipates energy in collisions, and allows energy transfer between rotational and translational modes. Recent theories (e.g. Jenkins & Richman 1985*b*; Lun & Savage 1987; Gutt 1987) account for these effects by assuming that the post-collision tangential component of the relative surface velocity of the colliding spheres is related to the pre-collision component by a constant tangential coefficient of restitution β, in analogy with the normal coefficient of restitution:

$$\boldsymbol{k}\times\tilde{\boldsymbol{u}}_{12} = -\beta(\boldsymbol{k}\times\boldsymbol{u}_{12}). \tag{5}$$

For real particles, β is not constant, but varies between the theoretical limits of -1 and $+1$, depending on the particular collision geometry and material properties of the particles.

Boundary conditions at solid and free surfaces must be specified to solve practical granular flow problems. Available theories for the boundary conditions at a solid surface (e.g. Jenkins & Richman 1986; Gutt & Haff 1988; Richman & Chou 1989) presently treat only frictionless particles, and are therefore of limited utility for experimental comparisons.

Free-surface boundary conditions on the stress tensor and flux of fluctuation energy are required to solve for the flow down an inclined plane. Johnson, Nott & Jackson (1990) proposed a set of conditions for flows having both well-defined and diffuse free surfaces. As will be seen, applying such theories to flows having a diffuse free surface is potentially complicated by air drag.

1.2. *Experimental observations*

Pre-kinetic-theory experimentation focused on engineering applications of chute flows of granular material. Much of this work, summarized in reviews by Savage *et al.* (1982) and Savage (1982, 1984) forms a qualitative foundation for theoretical development, but offers little quantitative information to test theories. More recently, Johnson *et al.* (1990) produced a well-documented set of experiments and a theory incorporating both frictional and collisional behaviour. They measured bulk-flow properties from the experiments for comparison with their theoretical predictions. Computer simulations of granular assemblages (e.g. Walton 1983; Campbell & Brennen 1985; Walton & Braun 1986*a*, *b*; Werner & Haff 1986; Walton & Drake 1988) providing a wealth of particle-scale information have supplemented information from physical experiments; however, properly validating and calibrating the computer models still depends on particle-scale observations of physical flows.

Few measurements of individual particle motions have been made in granular flows that are clearly collisional. Drake & Shreve (1986) presented the first particle-by-particle measurements of rapidly flowing identical spheres in an essentially two-dimensional inclined chute slightly wider than one particle diameter. They obtained profiles of bulk density and mean and fluctuating downstream and bed-normal velocities from high-speed motion pictures of a single disperse, collision-dominated flow. Ahn (1989) used fibre-optic probes pointed through a lucite sidewall to measure the downstream components of the mean velocity, the velocity fluctuation and the linear particle spacing of glass beads flowing in an inclined aluminium chute.

2. Two-dimensional experimental approach

Experiments designed to test grain-flow theories and computer simulations must allow observation of individual particle motions while minimizing the effects of extraneous forces within the experimental apparatus. Because observing individual particle motions in the interior of three-dimensional flows is difficult, an effectivc alternative is to study two-dimensional flows. Although the results of two-dimensional experiments cannot be directly applied to three-dimensional flows, they preserve the essential physics of the collisional processes that occur in all grain flows. This section describes the experimental apparatus and procedure, and addresses concerns about the extraneous forces and the degree of two-dimensionality in the experiments.

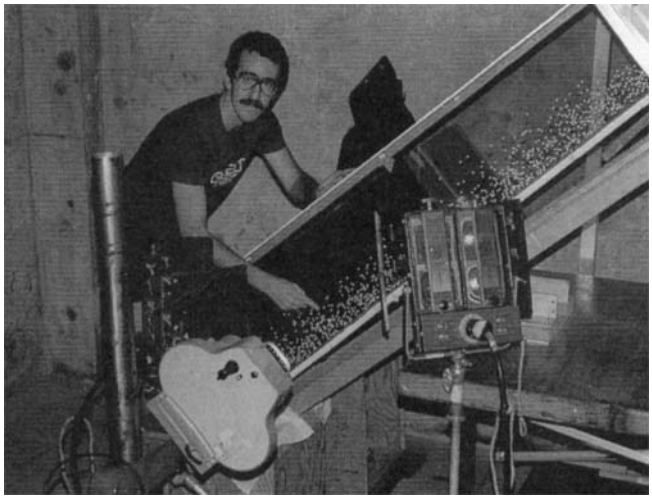

FIGURE 1. A typical disperse flow in the 3.7 m long, 0.5 m deep and 6.7 mm wide experimental chute. Plastic spheres 6 mm in diameter contained in a hopper above and behind the upper end of the apparatus feed onto a gently inclined tray, organizing into a single layer that spills into the head of the chute, where they form an essentially two-dimensional grain flow. The bed for the flows is the light-coloured strip inside the chute, which can be independently adjusted through a small range of angles to fine-tune the inclination. The flows approach a nominally steady, uniform condition rapidly, typically in 10–15 flow depths. A 16 mm camera operating at about 1440 frames per second or 60 times the normal projection rate documents particle motion; the centre of the camera field is about 70 cm upstream of the chute outlet.

2.1. *Description of apparatus*

Flows of 6 mm diameter spherical particles were generated in a glass-walled chute 3.7 m long, 0.5 m deep and just 6.7 mm wide (figure 1), confining the motion of the particles to essentially two dimensions, except for their spins. The chute could be inclined at any angle; and within it the bed could be moved independently to fine-tune the inclination. The principal experimental particles were nominal 6 mm diameter cellulose acetate spheres which were smooth, white, highly spherical and uniform in both size and density (Appendix A). Each was randomly imprinted with about 15 small black dots to enable the measurement of particle spins. Measurements of the normal coefficient of restitution ϵ for the experimental particles are described in Appendix B; over the range of experimental conditions $\epsilon = 0.84 \pm 0.01$.

The fixed bed (figure 2), intended to simulate naturally occurring beds of geophysical interest, consisted of immovable 6 mm spheres identical to those in the flows glued to the top of a stiff aluminium bar with randomly spaced gaps between them uniformly distributed over the range 0–5 mm, so that the moving particles could not touch the bar.

Flows were generated by placing about 15000–30000 spheres in a wide, V-shaped hopper above and to one side of the upstream end of the chute. They fed onto a slightly inclined, smooth tray, where they organized into a single layer that spilled over the edge of the tray and fell vertically between the glass walls to the chute bed. The flux of particles was controlled by blocking portions of the layer on the tray.

The flows were photographed about 0.7 m upstream of the chute outlet using a Hycam II 16-mm camera (Redlake Corp. Morgan Hill, CA) operating at a nominal rate of 1440 frames per second, or 60 times the normal projection speed. Two banks of 4-light Molefay Spotlights (Mole-Richardson Co. Hollywood, CA) frontally

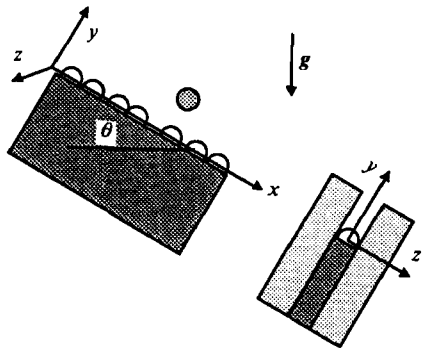

FIGURE 2. The fixed bed consists of 6 mm diameter cellulose acetate spheres like those in the flows glued on a rigid aluminium bar centred between the glass sidewalls. Gaps between bed particles are uniformly distributed on the interval 0–5 mm so that moving particles cannot touch the bar. Coordinate system for measurements in the glass-walled chute inclined at an angle θ to the horizontal; $\boldsymbol{g}$ is the gravitational acceleration. The bed-normal y-coordinate originates at the centreline of the fixed bed spheres, the x-coordinate extends downstream parallel to the bed, and the z-coordinate is perpendicular to the glass sidewall such that a particle rolling downhill has rotation $\omega_z < 0$.

illuminated the white particles against a black background. The films were analysed frame by frame to determine positions of the centres of the spheres and dots in machine-readable form by projecting the film image onto a digitizing tablet. Details of data-gathering and analysis are found in Appendix C.

2.2. *Experimental concerns*

Present grain-flow theories account only for body forces and forces generated by binary particle collisions, whereas extraneous forces such as air drag, friction of the spheres against the chute sidewalls and electrostatic forces may arise in the laboratory. The experiment was designed to minimize these extraneous forces: the open construction of the glass-walled chute and the spherical particle shape (as opposed to disks) minimized pneumatic effects due to the trapping of air; the largely two-dimensional particle motion minimized the normal forces, and hence the frictional effects, of impacts against the walls; and the large particle size minimized electrostatic effects. The degree of two-dimensionality attained in the experiments is an important additional concern, yet is difficult to address experimentally.

Simple models of the extraneous forces were used in conjunction with results from ancillary experiments to quantitatively estimate the magnitude of the forces affecting particle motions in the flows. Conservative over-estimates of the forces were used where detailed models were unavailable. The effects of extraneous forces were evaluated by comparing the volume rate of energy expended working against each force to the energy consumed in collisions between particles. The calculations also yield predictions of the out-of-plane translational motion in agreement with computer simulations of the flows (Walton & Drake 1988).

2.2.1. *Air drag*

The relative motion of spheres and air in the glass-walled chute exerts viscous drag forces on the spheres. Smoke was injected into several flows to visualize and roughly quantify air motion in the glass-walled chute. The flows were identical to those filmed for detailed analysis, and had a nominal depth of about 10 cm and a maximum depth of about 12 cm; they thus occupied roughly the lower third of the available chute height. The end of a narrow tube was positioned about 2 cm above the flowing

particles and cigar smoke was injected by gently puffing into the tube, which was then withdrawn to ensure unimpeded air motion throughout the chute. The smoke marked a circular parcel of air about 10 cm in diameter when injected into still air in the empty chute.

Smoke injected into the flowing particles was rapidly mixed throughout the depth of the flow and advected downstream. A distinct boundary separating clear air above from smoky air below was located at approximately the maximum height of the flowing particles; smoke released about 10 cm above the top of the particle layer in other experiments moved downstream very slowly, indicating that most of the air motion above the particle layer occurs within a few centimetres of the maximum height of the moving particles. In the particle layer the maximum velocity of the smoke-marked air occurs about 5 to 7 cm above the bed, determined from observations about 20 cm downstream of the injection site. Reliably timing the passage of the smoke over this short distance proved difficult, while over longer distances dispersion of the smoke within the particle layer prevented visualization. However, the leading edge of the slower-moving, relatively dense smoke just above the nominal free surface of the flow was timed over a one-metre distance; the mean velocity determined from three measurements is 1.6 m s^{-1}, roughly half the mean flow velocity at that height, and is a lower-bound estimate of the maximum air velocities in the chute.

The drag force $\boldsymbol{F}_D$ is assumed to be of the form (Batchelor 1967, p. 339)

$$\boldsymbol{F}_D = -\tfrac{1}{8} C_{drag} \rho_{air} \pi \sigma^2 |\boldsymbol{U}_{rel}| \boldsymbol{U}_{rel} \tag{6}$$

where ρ_{air} is the density of air, σ is the particle diameter, $U_{rel} = U - U_{air}$, U is the mean downstream particle velocity, U_{air} is the air velocity and the effective drag coefficient C_{drag} is assumed to be the result of air drag only. An analysis of twenty trajectories of particles saltating singly through essentially still air in the glass-walled chute gives $C_{drag} = 3.4 \pm 2.2$. For comparison, $C_{drag} = 0.5$ for a 6 mm diameter sphere falling at 2 m s^{-1} in still air with no nearby sidewalls (Stringham, Simons & Guy 1969, p. C33). The effective drag coefficient appears to be independent of velocity (figure 3); the scatter is due primarily to measurement error and the relatively short trajectories analysed, and to a lesser extent to sidewall friction, which is discussed in detail later.

The importance of air drag in the experimental flows can be evaluated by comparing the rate of energy loss per particle due to air drag, ΔE_D, with that due to collisions, ΔE_C (figure 4). The air-drag loss rate is

$$\Delta E_D = U |\boldsymbol{F}_D|, \tag{7}$$

where U is the mean downstream velocity of the particles. Taking

$$U_{air}(y) = \begin{cases} U_0, & y > y_0, \\ U_0 y / y_0, & 0 \leqslant y \leqslant y_0, \end{cases} \tag{8}$$

from the smoke experiments ($U_0 = 1.6$ m s^{-1}, $y_0 = 0.06$ m) conservatively overestimates U_{rel} and thus ΔE_D. The collisional loss rate is approximately

$$\Delta E_C \approx \tfrac{1}{4} m \overline{v^2} (1 - \epsilon^2) \zeta, \tag{9}$$

where $\overline{v^2}$ is the mean-square relative velocity of colliding particles. The collision rate ζ is taken to be the mean speed divided by the mean free path. Estimates of ΔE_C (figure 4) were calculated using a simple model based on elementary kinetic theory, which predicts measured collision rates in the flows reasonably well.

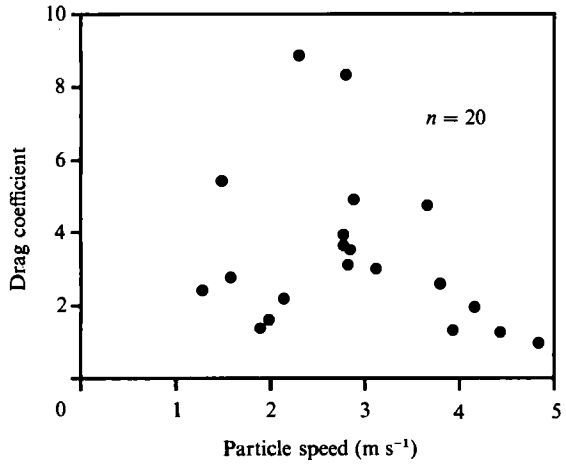

FIGURE 3. The drag coefficients determined by analysis of 20 particle trajectories in still air in the glass-walled channel are independent of particle velocity. The mean drag coefficient is 3.4 ± 2.2, or about 7 times the value for a 6 mm diameter sphere falling in unbounded still air at 2 m s^{-1}.

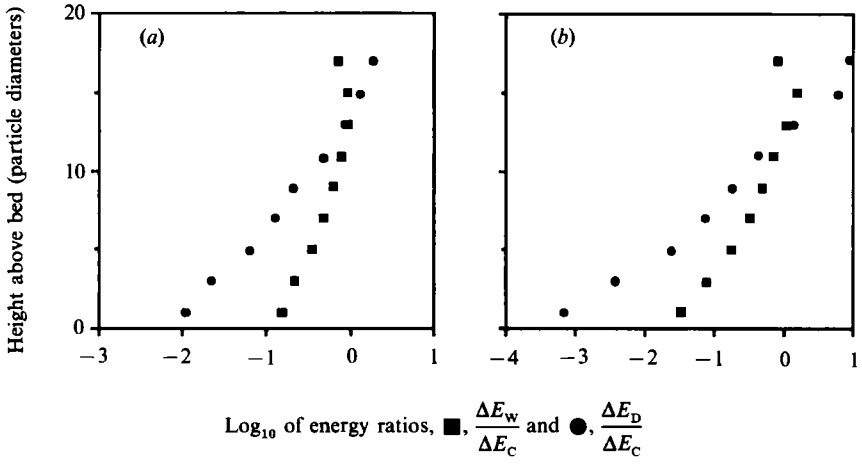

FIGURE 4. Conservative estimates of the ratios of the rates of energy dissipated by extraneous forces and energy dissipated by anelastic collisions in (*a*) disperse and (*b*) dense flows. ΔE_W, ΔE_D, and ΔE_C are the dissipation rates due to sidewall friction, air drag and particle–particle collisions.

In both disperse and dense flows collisional energy losses clearly overwhelm air-drag losses near the bed, where collision rates are high and particles move slowly relative to air in the chute. Near the free surface of the flow, although more energy is dissipated by air drag than by collisions on a per-particle basis, neither mechanism effectively dissipates much flow energy because the density of particles is so low. This implies that the small number of drag-affected particles near the top of the flow are relatively inconsequential to the overall flow dynamics.

The presence of air in the chute has one other potential effect on the flows. Work done squeezing air from between colliding particles may increase collisional energy losses, although any cushioning effect is probably extremely small due to the small contact area of colliding spheres and the high permeability of the flows. Because the errors in digitizing particle positions prevent measurement of decelerations over distances less than about 10 particle diameters, the energy losses calculated for sphere collisions include any losses due to air cushioning.

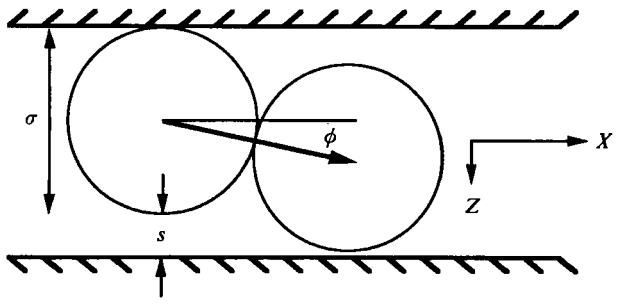

FIGURE 5. Simplified binary collision geometry in the glass-walled channel is described by the small collision angle ϕ between a plane parallel to the glass sidewalls and the line connecting the particle centres at impact. The particle diameter is σ and the channel width is $\sigma + s$. See text for simplifying assumptions.

2.2.2. *Sidewall friction*

It is difficult to determine experimentally the effects of friction against the glass sidewalls. Departures from ideal two-dimensionality strongly influence the magnitude of frictional forces generated by collisions between the particles and the walls. Calculations based on simple physical models presented below predict the typical magnitude of the out-of-plane velocity component and its dependence on the ratio of the chute width to particle diameter, and constrain the magnitudes of the frictional forces and energy lost through particle–sidewall collisions. The calculations predict out-of-plane velocities and sidewall normal stresses in agreement with preliminary computer simulations of the experimental flows (Walton & Drake 1988).

Casual observation of dotted particles in flows reveals several fundamental features of the spin motion of the particles useful in building a model of particle–sidewall interactions: the direction of the spin axis is non-uniformly distributed in three-dimensional space, though typically particles spin as if rolling downhill; spins change visibly only during collisions between particles; and, in a significant number of particle collisions, additional collisions between the particles and chute sidewalls must be inferred to explain the post-collision particle motion. The total collisional change in spin kinetic energy can be directly measured from the films, as can those parts of the translational kinetic energy that lie in the plane of the chute, but the portion of the kinetic energy transferred into out-of-plane translational motion is unknown. Because the obvious transfers of energy to and from this invisible reservoir occur during collisions between particles, the analysis focuses there first.

If the flow is fast and disperse and the particles sufficiently anelastic so that free paths between collisions are long enough for the out-of-plane velocity component to be reduced by wall collisions, the motion of individual particles between collisions is nearly two-dimensional and contained in a plane nearly parallel to the sidewall, and the surface velocity of the particles due to spin is small compared to the translational particle speed. Under these conditions, the essential geometry of a binary collision (figure 5) is described by the small collision angle ϕ between a plane parallel to the glass sidewalls and the line connecting the particle centres. Then, assuming that particle trajectories are uniformly distributed across the width of the gap, the root-mean-square collision angle Φ obtained by integrating over all collision angles is

$$\Phi = \frac{s}{\sqrt{3}\sigma}, \tag{10}$$

where s is the difference between the chute width and the particle diameter σ. The typical average speed w_0 normal to the sidewalls immediately following a particle–particle collision can be found by applying conservation of linear momentum to the collision of two particles at angle Φ to the sidewalls. The colliding particles are assumed to have a normal coefficient of restitution ϵ and to travel parallel to the sidewall before impact with velocities u_1 and u_2, where $|u_1-u_2| = (2T)^{\frac{1}{2}}$ is a typical relative speed of colliding particles ($2T$ is the mean-square fluctuating particle speed). Then

$$w_0 = |w_1| = |w_2| = \tfrac{1}{2}(1+\epsilon)\cos\Phi\sin\Phi\,|u_1-u_2|, \tag{11a}$$

$$\approx \frac{(1+\epsilon)}{\sqrt{2}}\Phi T^{\frac{1}{2}}. \tag{11b}$$

This speed is reduced by a factor ϵ at each sidewall collision, which can result in a significant reduction when the mean free path is long and many sidewall collisions occur. Assuming the particle–particle and particle–glass coefficients of restitution are equal, the average transverse speed $\bar{w}$ between particle–particle collisions is

$$\bar{w} = \frac{w_0}{\gamma}\frac{\ln[\gamma(1/\epsilon)-1)+1]}{\ln(1/\epsilon)}, \tag{12}$$

where

$$\gamma = \frac{w_0\xi}{s(2T)^{\frac{1}{2}}}, \tag{13}$$

is the ratio of the initial sidewall collision rate to the particle–particle collision rate, and ξ is the mean free path. Using typical experimental values of $(2T)^{\frac{1}{2}} = 0.7$ m s^{-1}, $\xi = 0.06$ m, $\epsilon = 0.84$ and $\Phi = 0.067$ (corresponding to a chute width of 6.7 mm) in (11), (12) and (13) gives $w_0 = 0.04$ m s^{-1}, $\gamma = 5$ and $\bar{w} = 0.03$ m s^{-1}. Including the effects of interparticle friction, for example, by allowing no relative tangential surface velocity after impact, decreases $\bar{w}$ by about 15%.

In computer simulations of the experimental flows (O. R. Walton, personal communication, 1987) using $\Phi = 0.024$ (chute width 6.25 mm), typical instantaneous values of w ranged from millimetres per second to a maximum of 0.06 m s^{-1}; the r.m.s. value of w was not calculated. For similar conditions, the model predicts $\bar{w} = 0.02$ m s^{-1}, taking the root-mean-square fluctuating speed of 0.8 m s^{-1} in the simulation as a typical relative velocity at collision. Walton's simulation also calculates the mean normal stress exerted on the sidewall, P_{zz}, by averaging the forces of individual impacts of particles over unit area and time. Using the approximate relation

$$P_{zz} = \frac{\rho\bar{w}^2}{s}, \tag{14}$$

where ρ is the mean areal flow density from the simulation, provides another estimate of $\bar{w} = 0.034$ m s^{-1}, in rough agreement with $\bar{w} = 0.02$ m s^{-1} predicted by the model.

The maximum magnitude of the frictional forces arising from particle–sidewall collisions and the energy expended working against them can be estimated by assuming that the particles slide against the sidewall throughout the duration of the collision. The frictional force opposing the sliding motion is

$$F_w = \mu F_n \approx \mu\left(2m\frac{\bar{w}}{t_c}\right), \tag{15}$$

where μ is the coefficient of sliding friction, m is the particle mass and t_c is the collision duration. The energy dissipated per sidewall collision by sliding friction

$$F_w U t_c \approx 2\mu m \bar{w} U \tag{16}$$

is independent of the collision duration. Then the energy dissipated per particle per unit time is

$$\Delta E_w = \frac{1}{3}\left(\frac{1+\epsilon}{\sigma\gamma}\right)^2 \left\{\frac{\ln[\gamma((1/\epsilon)-1)+1]}{\ln(1/\epsilon)}\right\} \mu m s U T. \tag{17}$$

Near the bed collisional losses are typically one to two orders of magnitude greater than wall-friction losses (figure 4). The ratio of wall-friction to collision losses has a broad maximum a few particle diameters below the maximum flow height; above this region trajectories are tens to hundreds of particle diameters long and are adequate to reduce $\bar{w}$ and wall-friction losses significantly. Near the top of the flows the ratio of wall-friction to air-drag losses is 37% for the disperse flow and only 9% for the dense flow, indicating that some of the scatter in the measurements of the effective air-drag coefficient can be ascribed to wall friction. Finally, some additional calculations using these estimates of the wall friction are consistent with observations of near-constant particle spin over trajectories with long free path. In particular, the spins that are generated by sliding at particle–sidewall contacts are generally smaller than the typical errors in measuring spins.

When the tangential component of the contact force F_w between particle and sidewall is the same as μ times the normal component F_n, the particle slides and the resultant torque induces spin. If F_w is less than μF_n, on the other hand, sliding does not occur. Particles are not perfectly rigid, of course, so, although the particle does not slide, it does not instantaneously acquire a spin corresponding to pure rolling motion. The details of the contact interaction are complex (e.g. Mindlin & Deresiewicz 1953), and it suffices to indicate that both sliding and sticking contact can occur on different parts of the contact surface, even simultaneously, during the course of a single collision.

The angular acceleration α due to the torque applied during sliding is

$$\alpha = \frac{\sigma F_w}{2I}, \tag{18}$$

where, from (15),

$$\tfrac{1}{2}\sigma F_w = \tfrac{1}{2}\sigma\mu \frac{2m\bar{w}}{t_c}, \tag{19}$$

and the moment of inertia I of a homogeneous sphere is

$$I = \tfrac{1}{10} m\sigma^2. \tag{20}$$

Then, assuming the initial spin to be zero, the spin ω_s imparted by sliding is

$$\omega_s = \alpha t_c = \frac{10\mu\bar{w}}{\sigma}. \tag{21}$$

In the upper part of disperse flows the mean sidewall-normal speed $\bar{w}$ is about 0.01 m s^{-1}, which implies values of ω_s around 3 rad s^{-1}; a typical error in determining the spin is about 4 rad s^{-1} (Appendix C). Even in dense flows where $\bar{w}$ and ω_s are higher the changes in spins between particle–particle collisions are essentially impossible to determine experimentally, because the spin errors are inversely proportional to the measurement interval, which in turn must be made as short as possible to detect any wall-induced changes in ω_s occurring between particle–particle collisions.

2.2.3. *Electrostatic forces*

Electrostatic forces may be generated by plastic particles moving along the glass sidewalls, which presumably transfers charge from the particles to the glass or *vice versa*. No signs of electrical charge transfer, such as unusual dust accumulation on the particles and glass chute or static discharge, were ever observed.

Simple calculations determine the maximum charge a particle can carry before the surrounding air undergoes dielectric breakdown; then the electrostatic potential energy needed to hold two such charged particles in contact can be compared to the typical maximum elastic energy stored in colliding particles. The charge accumulated on the glass sidewalls should be of similar sign and magnitude on either side of the chute, so that no gradient in electric field exists within the chute. Then the principal electrostatic forces are repulsive forces arising from the similar charges accumulated on particles. The order-of-magnitude estimate sought here ignores the polarization forces which arise when a charged particle is brought near a dielectric material such as glass; these forces are at most comparable to interparticle electrostatic forces, and probably much smaller. The field E at distance r outside a uniform sphere holding a charge Q (ignoring the presence of the glass sidewalls) is

$$E = \frac{kQ}{r^2}, \tag{22}$$

where $k = 9 \times 10^9$ N m^2 C^{-2} is the Coulomb constant. Typical values of the maximum electric field generated by friction in the pneumatic transport of fine plastic particles are about 150 kV m^{-1} (Cartwright, Singh & Bailey 1985, p. 546), about 20 times less than the field at which air spontaneously ionizes, or about 3 MV m^{-1}. Conservatively setting $E = 3$ MV m^{-1} and $r = 3 \times 10^{-3}$ m gives $Q = 3 \times 10^{-9}$ C, and the work needed to bring a sphere of diameter σ with charge Q from an infinite distance into contact with a second sphere having equal charge is

$$W = \frac{kQ^2}{\sigma}. \tag{23}$$

This work, which represents the electrostatic potential energy available to repel the spheres, is about one-third the typical elastic energy stored in the spheres at their maximum compression during impact. Under typical conditions the ratio of the electrostatic to elastic potential energies is likely to be orders of magnitude smaller; and thus electrostatic effects are almost surely negligible in the experiments.

3. Detailed profiles of two collisional flows

Detailed profiles of mean and fluctuating quantities were obtained from films of two nominally steady, uniform flows having fluxes of about 1280 and 2230 particles s^{-1}. The flows exemplify the disperse and dense end-member cases treated by kinetic theories of grain flow. The theory of Lun *et al.* (1984) and the computer simulations of Walton & Braun (1986*b*) for smooth, anelastic spheres in simple three-dimensional shear flows show that the collisional contribution to the stress tensor dominates the kinetic or transport contribution at solids *volume* fractions greater than about 0.15. Simulations of two-dimensional shear flow by Walton & Braun (1986*a*) using frictional disks show that the two contributions are comparable in magnitude at a solids *area* fraction of about 0.3; these figures roughly correspond to bulk densities of about 1.6 kg m^{-2} in the present experiments (figure 6). Thus, in the disperse 1280-

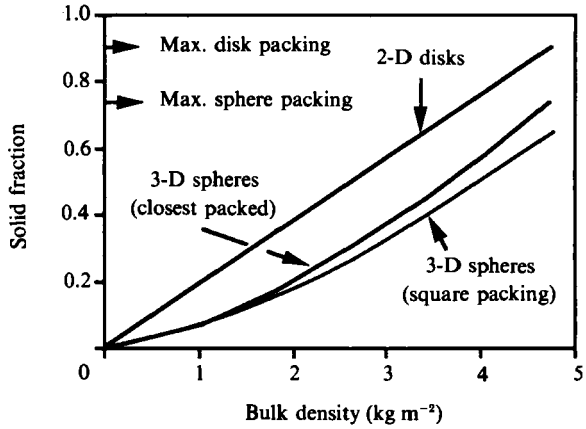

FIGURE 6. Relation between the experimental bulk density and three measures of particle concentration in two- and three-dimensional flows. The experimental bulk density is determined by counting the number of spheres per unit area and multiplying by the mass of a sphere; alternatively, multiplying the number of spheres by the projected area of a sphere gives a two-dimensional solid fraction analogous to that typically determined for flows of disks. A rough transformation from two- to three-dimensional solid fractions can be derived by equating the distance between the centres of neighbouring particles during homogeneous areal expansion of a square lattice of disks, to the analogous distance between neighbouring spheres in a cubical lattice, which gives $\nu_{2D} = (\frac{2}{3}\pi^{\frac{1}{2}}\nu_{3D})^{\frac{2}{3}}$ (Campbell & Brennen 1985); alternatively, homogeneous expansion of two- and three-dimensional hexagonal close-packed arrays of particles gives $\nu_{2D} = (\frac{1}{2}3^{\frac{1}{2}}\pi^{\frac{1}{2}}\nu_{3D})^{\frac{2}{3}}$, which ensures that the maximum two-dimensional packing corresponds to the maximum three-dimensional packing.

particles s^{-1} flow the kinetic contribution to the stress tensor is much greater than the collisional contribution over nearly the entire flow depth, while in the dense 2230-particles s^{-1} flow the collisional contribution dominates in that part of the flow extending from the bed up to about 10 particle diameters.

For both flows the bed consisted of randomly spaced 6 mm diameter spheres, and the chute inclination was 42.75°. This inclination provides relatively long-duration flows which are nearly steady and uniform and have the optimal combination of moderate bulk density and high total flux. At low bulk densities the particle velocities are relatively high, and thus require high filming rates, substantially reducing the period of observation and in turn, the number of individual observations of particles from which statistics are calculated. Furthermore, the potential influence of undesirable air drag increases with decreasing mean bulk density, because less air is entrained within the flowing mass of particles and the relative velocity between air and particles is increased. At high densities the short mean free path between collisions prohibits accurate measurement of intercollision particle velocities and complicates counting of collisions.

Given the relatively large inherent fluctuations in flow properties in small granular systems, demonstrating a flow to be steady and uniform is a difficult experimental task. Ideally, flow steadiness and uniformity should be assessed by comparing profiles of mean and fluctuating particle velocities and spins determined at two stream-wise distant points in a flow for a suitably long time, but several practical problems prevent such a comparison. Instead, therefore, the camera field was split into upstream and downstream portions, the filming interval was divided in half, and the density-weighted mean downstream (u) and bed-normal velocities (v) and particle flux were calculated for the four subsets of the data for each film (table 1).

Disperse flow (1280 *particles/s*)				
Dataset subset	u (m/s)	v (m/s)	Flux (particles/s)	Observations
Upstream half of field	2.13 ± 0.06	-0.01 ± 0.05	1162	755
Downstream half of field	2.15 ± 0.06	-0.03 ± 0.05	1394	900
First half of film	2.19 ± 0.07	-0.02 ± 0.05	1293	824
Second half of film	2.09 ± 0.06	-0.02 ± 0.05	1262	831
Dense flow (2230 *particles/s*)				
Data subset	u (m/s)	v (m/s)	Flux (particles/s)	Observations
Upstream half of field	1.75 ± 0.03	-0.02 ± 0.02	2184	1499
Downstream half of field	1.76 ± 0.04	-0.01 ± 0.02	2246	1530
First half of film	1.81 ± 0.03	-0.01 ± 0.02	2275	1557
Second half of film	1.70 ± 0.03	-0.02 ± 0.03	2153	1472

TABLE 1. Mean velocities and flux for subsets of the data

The data for the disperse flow consists of 37 independent ensembles of particle positions, velocities and rotations taken at 100 frame intervals (0.065 s) over the constant-filming-rate portion of the film; data for the dense flow comprise 31 such ensembles.

Computing the velocities and rotations of individual particles and the density of the flow from the location of particle centres and dot positions on film frames is conceptually straightforward, although it entails numerous practical difficulties. A Cartesian coordinate system (figure 2) is set up with origin located on the line of centres of the fixed bed spheres and axes oriented upward normal to the bed and downstream parallel to it. The useable field of view in each film was about 8.35 cm in the bed-parallel (x) direction and 11.1 cm in the bed-normal (y) direction; the centre of the field was about 70 cm upstream of the chute outlet. The flow is divided into bed-parallel layers or bins two particle diameters thick, and the desired quantities are calculated for each bin. All of a particular particle property (e.g. its mass) is applied to the bin containing the particle centre. The area of the bin nearest the bed used to calculate the bulk density excludes that area unavailable to the centres of flow particles. The excluded area is computed assuming the bed-sphere centres are uniformly spaced a distance equal to the mean of the true spacing distribution.

3.1. *Profiles of mean quantities*

3.1.1. *Bulk density*

The bulk density (figure 7*a*) decreases approximately linearly with distance from the bed in both flows, forming a diffuse free surface about 18 particle diameters above the bed. Occasional particles passed above the camera field of view (visually estimated during filming to be about 2–3 particles in 20000).

3.1.2. *Collision rates*

Collision rates for each bin (figure 7*b*) were determined by selecting the upstream-most wholly visible particle whose centre lay within the bin of interest, and counting its collisions with other particles until its centre left the bin. Then another particle was selected according to the above criteria. In the three bins nearest the bed in the dense flow many collisional encounters appeared to involve more than two particles; one consequence of the short free paths and limitations on the filming rate and film

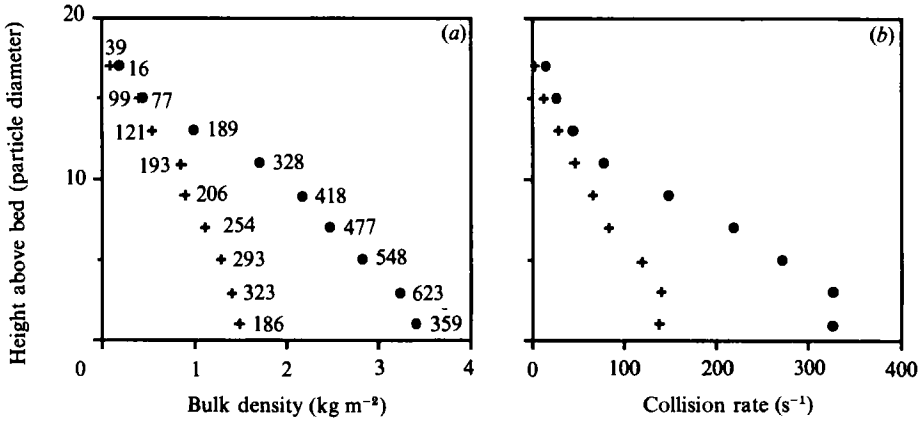

FIGURE 7. (*a*) Bulk density profiles for flows having fluxes of ●, 2230 particles s^{-1} and +, 1280 particles s^{-1} in 2 particle diameter thick bins. Number of spheres counted to determine density is indicated next to data points. (*b*) Collision rates for the same flows, determined by counting the number of collisions for single particles selected at the upstream end of bins; collision counts for each selected particle ended when the particle left the bin, and a new particle was selected. Total sample time ●, 1.35 s; +, 1.38 s. Only particle–particle collisions are given for the near-bed bin; the particle–bed collision frequency per unit length of bed (not shown) was determined independently by counting the number of flow particles contacting each fixed bed particle along a 7.9 cm long segment of the bed for a given time interval. The measured rates were 110 collisions cm^{-1} s^{-1} for the dense flow (0.74 s observation), and 13 collisions cm^{-1} s^{-1} for the disperse flow (2.41 s observation).

resolution is that the reported rates may underestimate the true rates in these bins. Particle–particle and particle–bed collisions were distinguished in the bin nearest the bed. In addition, the particle–bed collision frequency per unit length of bed was determined independently by counting the number of flow particles contacting each fixed bed particle along a 7.9 cm long segment of the bed for a given time interval. The measured rates were 110 collisions cm^{-1} s^{-1} for the dense flow (0.74 s observation), and 13 collisions cm^{-1} s^{-1} for the disperse flow (2.41 s observation).

3.1.3. *Mean velocities*

The mean downstream and mean bed-normal velocities for the disperse and dense flows are shown in figure 8. The downstream velocity profiles are nearly parallel and differ only in the slip velocity at the bed, which is about 0.7 m s^{-1} for the disperse flow and about 0.3 m s^{-1} for the dense flow. The mean bed-normal velocities in each bin are less than 1% of the corresponding downstream velocities except in the bin nearest the bed, where the mean bed-normal velocity is directed towards the bed and equals about 14% (disperse flow) and 7% (dense flow) of the downstream velocity. Computer simulations currently in progress (Walton & Drake 1988) may provide an explanation of this behaviour.

3.1.4. *Mean rotations*

Mean particle rotation vectors ($\bar{\omega}$) are predominantly oriented perpendicular to the chute sidewalls. The mean out-of-plane components $\bar{\omega}_x$ and $\bar{\omega}_y$ (figure 9) due to particle–sidewall impacts and non-coplanar particle–particle collisions are typically much smaller than the in-plane component $\bar{\omega}_z$ (figure 10); for the dense flow the flow-average ratios of $\bar{\omega}_x$ and $\bar{\omega}_y$ to $\bar{\omega}_z$ are 0.11 and 0.05, and for the disperse flow the same ratios are 0.06 and 0.08. Lacking a theory predicting the rotational temperature

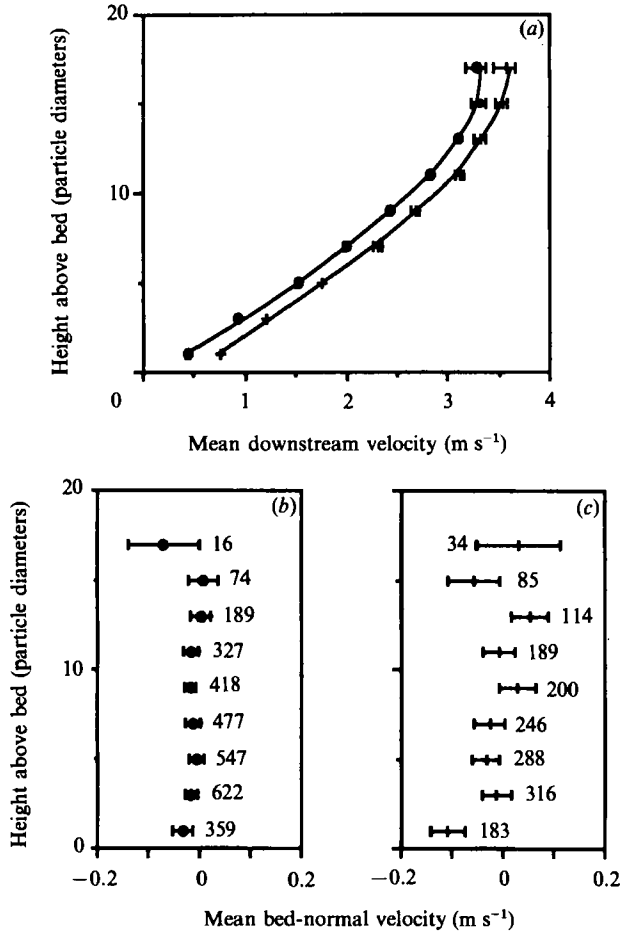

FIGURE 8. (*a*) Mean downstream velocity profiles for flows having fluxes of ●, 2230 particles s^{-1} and +, 1280 particles s^{-1}. Error bars indicate one standard deviation each way from the mean; bars on lower points are too short to plot. Curves are least-squares, best-fit cubic polynomials that enable determination of the velocity gradient. Number of velocity measurements for data points in (*a*) is the same as displayed in the bed-normal velocity profiles (*b*) and (*c*).

(proportional to the variance of the mean rotation measurements), it is difficult to meaningfully test the hypotheses that the mean rotations $\bar{\omega}_x$ and $\bar{\omega}_y$ were zero.

The mean in-plane rotations $\bar{\omega}_z$ (figure 10) are nearly equal to curl $\boldsymbol{u}$ throughout the dense flow, in agreement with the theories of Lun & Savage (1987) and Gutt (1988). In the disperse flow, the collisional contribution to the angular momentum flux can be ignored, and the difference between the mean spin and the rotational bulk deformation curl $\boldsymbol{u}$ is balanced by a gradient in angular momentum flux (Lun & Savage 1987):

$$c\frac{\mathrm{d}}{\mathrm{d}y}[\rho\langle v'\omega_z'\rangle] = -\xi\left(2\bar{\omega}_z + \frac{\mathrm{d}u}{\mathrm{d}y}\right), \tag{24}$$

where c is a constant depending on particle properties, the angle-bracketed term is the ensemble average of the product of the fluctuating bed-normal velocity v' and the fluctuating rotation ω_z', and ξ is the rotational viscosity. The measured gradients in ρ and the angle-bracket term are of the proper sign, in qualitative agreement with the theory.

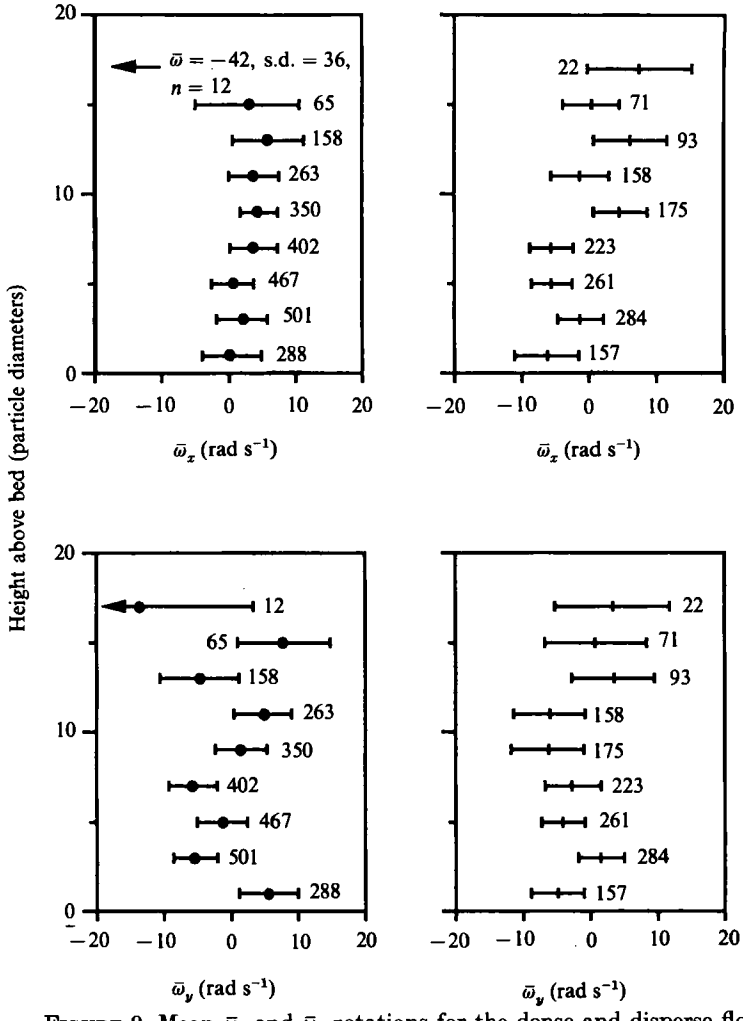

FIGURE 9. Mean $\bar{\omega}_x$ and $\bar{\omega}_y$ rotations for the dense and disperse flows. ●, 2230 particles s^{-1}; +, 1280 particles s^{-1}.

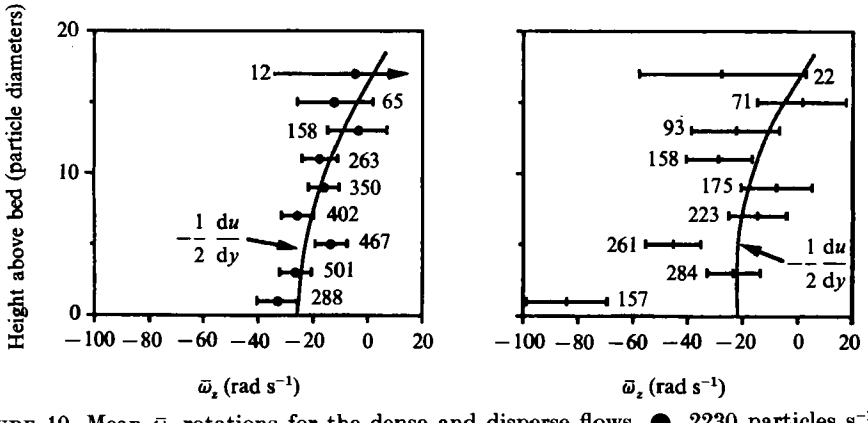

FIGURE 10. Mean $\bar{\omega}_z$ rotations for the dense and disperse flows. ●, 2230 particles s^{-1}; +, 1280 particles s^{-1}. The predicted rotation for simple homogeneous shear flow is shown by the curve $-\frac{1}{2}(du/dy)$, which is determined by differentiating the polynomial mimic function for the velocity profile shown in figure 8(*a*).

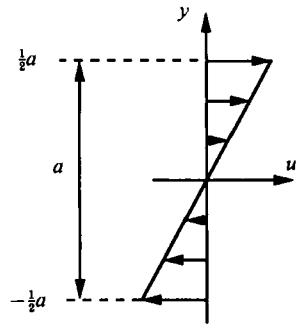

$$\langle u'^2\rangle^{\frac{1}{2}} = \frac{1}{a}\int_{-\frac{1}{2}a}^{\frac{1}{2}a}\left(\xi\frac{\mathrm{d}u}{\mathrm{d}y}\right)^2\mathrm{d}\xi$$

$$= \tfrac{1}{12}a^2\left(\frac{\mathrm{d}u}{\mathrm{d}y}\right)^2$$

FIGURE 11. Errors in fluctuating velocities due to binning measurements in bins of width a, across which the velocity gradient $\mathrm{d}u/\mathrm{d}y$ is constant. In a typical experiment, $a = 0.012$ m, $\mathrm{d}u/\mathrm{d}y = 50\ \mathrm{s}^{-1}$, and the r.m.s. u' due to binning is about $0.17\ \mathrm{m\ s}^{-1}$, or about 30% of the true r.m.s. u'.

3.2. *Profiles of fluctuating quantities*

Fluctuations in particle velocities and rotations are the chief microstructural variables of interest, because their distributions form the foundation for kinetic theories of grain flow. Experimentally, the fluctuations are the most difficult quantities to obtain because the sample size is typically small, and the concomitant uncertainty in the desired fluctuating quantities is large. Also, in flows having large gradients in mean quantities, partitioning the flow into bins can produce erroneous estimates of fluctuating components. In particular, the downstream velocity gradient is large, and simply subtracting the mean velocity for the bin from the instantaneous particle velocities to determine the fluctuating component gives misleading results. Figure 11 illustrates the dependence of the false fluctuations on the magnitude of the velocity gradient and bin size. A curve-fitting technique is used when the root-mean-square (r.m.s.) fluctuating component due to binning is comparable to the standard deviation of the component. Interpolation of a smooth polynomial passing through the mean velocities obtained for each bin provides the true mean velocity at the observed y-value corresponding to each instantaneous velocity measurement, from which the fluctuating component is calculated. The curve-fitting technique must be applied with caution when the datapoints for the mean quantity have large uncertainties; it is used here only on the downstream velocity profiles of the flows.

3.2.1. *Fluctuating velocities*

The distributions of each of the fluctuating components of velocity are approximately Maxwellian, while those of the rotations may deviate significantly from Maxwellian behaviour. In general, fluctuation energy is not equally partitioned among the available modes, as it would be in a flow of perfectly rough, elastic particles. In a two-dimensional flow of such spheres between frictionless sidewalls, one third of the fluctuation kinetic energy would reside in each of two translational modes and a single rotational mode. Incomplete frictional coupling of particles ($\beta \neq 1$) reduces the proportion of the total energy contained in the rotational mode (Lun & Savage 1987); furthermore, when the anelasticity of particle collisions and shear rate are sufficiently great, the energy contained in the two translational modes is generally not equal (e.g. Jenkins & Richman 1988). Both these effects are clearly evident in the experimental flows, as are additional effects caused by departures from ideal two-dimensionality, which siphon a small amount of fluctuation kinetic energy into the sidewall-normal translational mode and the out-of-plane rotational modes. Qualitative comparison between the experiments and theoretical predictions for

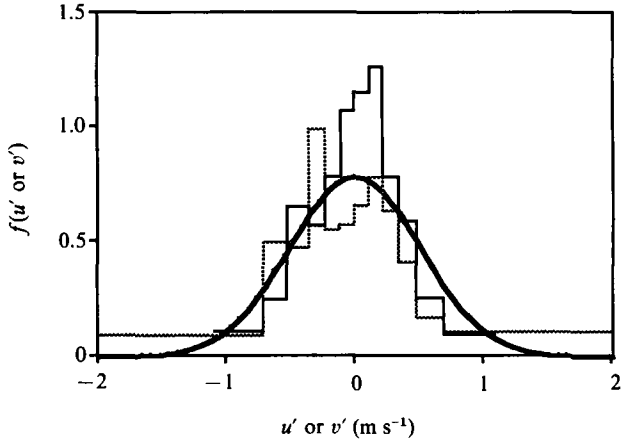

FIGURE 12. Typical distribution of fluctuation velocities. Disperse flow: $n = 114$; $y = 0.078$ m; r.m.s. $u' = 0.607$ m s^{-1}; r.m.s. $v' = 0.390$ m s^{-1}. —, u'; —— v'; ——, Maxwellian (T_t).

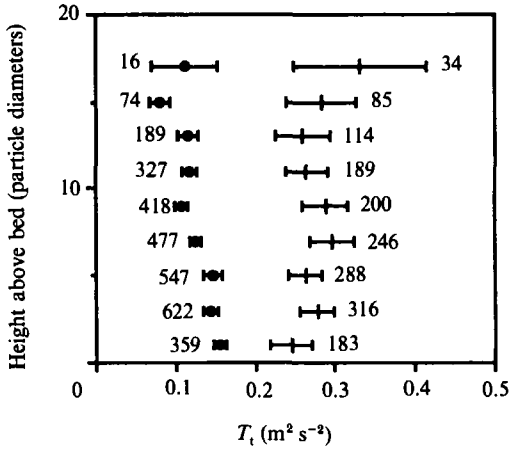

FIGURE 13. Profiles of the translational temperature T_t. In +, the disperse flow, the temperature is independent of depth ($T_t = 0.278$ m^2 s^{-2}), to within the statistical uncertainty; whereas in ●, the dense flow, a non-zero gradient in T_t at the bed implies that collisional dissipation is not sufficient to balance fluctuation energy generated by slip-work at the bed.

uniformly shearing flows can be made by examining the fluctuating quantities (denoted by primes) in a single bin, in which the flow approximates the theoretical ideal.

Typical distributions of the bed-parallel (u') and bed-normal (v') fluctuation velocities in a single bin are significantly different (figure 12). The differences are particularly prominent in low-bulk-density, high-shear regions of the flow; they arise because particles transported across the mean-flow velocity gradient in u acquire greater u' relative to v' merely by virtue of collisionless travel. The ratio of r.m.s. u' to r.m.s. v' is typically about 1.4 to 1.6 in both flows, except within 3 or 4 particle diameters of the bed, where the ratio is typically about 1.1 or less.

3.2.2. *Translational temperature*

Profiles of the translational temperature $T_t = \frac{1}{2}(\langle u'^2 \rangle + \langle v'^2 \rangle)$ are shown in figure 13. In the disperse flow the hypothesis that the temperature is independent of depth ($T_t = 0.278$ m^2 s^{-2}) cannot be rejected at the 95% confidence level; in the dense flow,

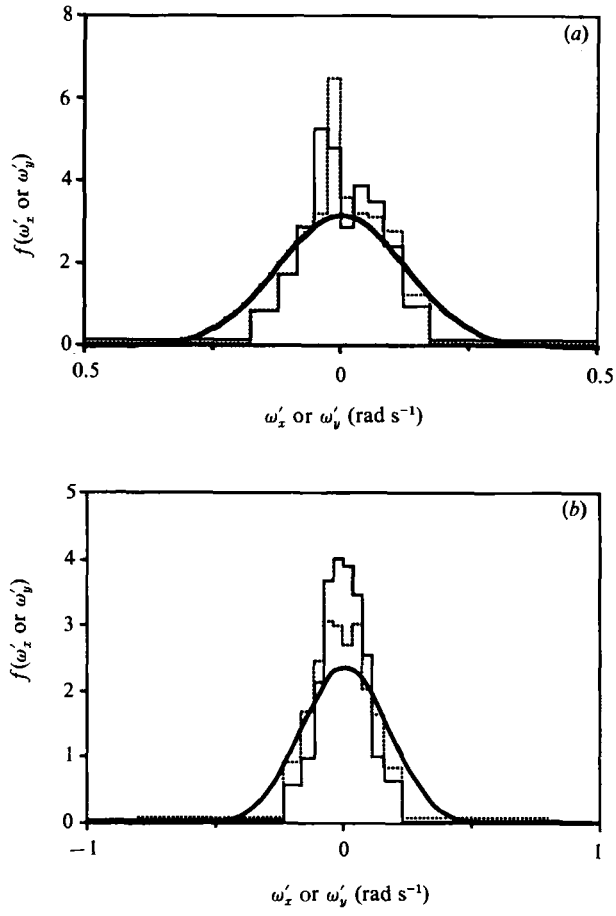

FIGURE 14. Distributions of the out-of-plane fluctuation rotations ——, ω_x' and — —, ω_y'. ———, Maxwellian (T_{rxy}). (*a*) $n = 158$, $y = 0.078$ m. In the disperse flow, both ω_x' and ω_y' are approximately the same throughout the flow depth, but display higher-than-predicted proportions of particles with both very-low-magnitude fluctuating rotations and relatively high ones. (*b*) $n = 501$, $y = 0.018$ m. In the dense flow ω_x' and ω_y' show a deficiency in particles with rotations of medium magnitude, as in the disperse flow, and the two distributions becomne increasingly different near the bed.

the temperature decreases approximately linearly with distance from the bed. The presence of a non-zero gradient in translational temperature at the bed in the dense flow implies that fluctuation energy generated by slip-work at the bed is not balanced by collisional dissipation, but diffuses into the body of the flow.

3.2.3. *Fluctuating rotations*

Fluctuating rotations in the two flows exhibit a surprising variety of phenomena. In particular, the distributions of the rotations deviate noticeably from a Maxwellian form. In the disperse flow, the distributions of ω_x' and ω_y' (figure 14*a*) are approximately the same throughout the flow depth, but display higher-than-predicted proportions of particles with both very-low-magnitude fluctuating rotations and relatively high ones. In such flows particles typically move at high velocity relative to the sidewalls, so that frictional interactions with the sidewalls are dominated by slip and only ineffectively generate particle rotations. Furthermore,

because particles typically travel at least several diameters between particle–particle collisions, any so-generated rotations are damped by numerous sidewall collisions. A few slow-moving particles apparently interact significantly with the sidewalls, however, and generate the large rotations in the tails of the distributions.

Distributions of ω_x' and ω_y' in the dense flow show a deficiency in particles with rotations of medium magnitude, as in the disperse flow. In addition, they are significantly different near the bed (figure 14*b*), with the differences decreasing with increasing distance from the bed. The differences result from collisions not non-coplanar with the experimental chute. If, for example, the vector connecting the centres of two colliding particles is parallel to the bed but at an angle to the chute sidewalls, the collision generates a rotation ω_y. For simplicity, the frictional effects of the particle–glass interactions can be neglected, because the coefficient of friction for particle–particle contact is approximately 1.5 to 2 times greater than the coefficient for particle–glass contact. Because r.m.s. u' is greater than r.m.s. v' at any point in the flow, the x-component of the mean relative velocity at collision is typically greater than the y-component, so that non-coplanar collisions generate rotations having $|\omega_y|$ greater than $|\omega_x|$. This simple picture applies near the bed, where the layered structure in the grain-layer-gliding zone (Drake 1990) produces a directional anisotropy in the vectors connecting centres of colliding particles, so that a large number of collision vectors are either parallel or perpendicular to the bed. Farther from the bed this anisotropy is considerably diminished; as a result, the distributions of ω_y' and ω_x' become more nearly identical with increasing distance from the bed.

Of greater theoretical interest is the z-component of the fluctuating rotations, which would be the only rotational mode in a truly two-dimensional flow. The distributions of ω_z' are approximately Maxwellian in both flows at distances greater than a few particle diameters above the bed (figure 15*a*). Nearer the bed, however, each flow exhibits a different type of non-Maxwellian behaviour.

In the bin nearest the bed in the disperse flow, the distribution of ω_z' (figure 15*b*) has approximately twice as many particles in the negative tail as in the positive one, a statistically significant difference. The asymmetry is produced by the large number of particle–bed collisions, which produce mostly large negative rotations, relative to the number of particle–particle collisions, which produce rotations having both positive and negative sign.

In the near-bed bin in the dense flow, particle–particle collisions dominate particle–bed collisions, and no asymmetry is evident. Within about 4 particle diameters of the bed, however, the distributions (e.g. figure 15*c*), are deficient in particles having medium-magnitude rotations, similar to the behaviour observed for ω_x' and ω_y' (figures 14*a*, *b*). As mentioned above, the layered structure in the grain-layer-gliding zone produces a directional anisotropy in the vectors connecting centres of colliding particles, so that a large number of collision vectors are either parallel or perpendicular to the bed and a bimodal mix of glancing and head-on collisions occur. Detailed models of particle collisions (Walton & Drake 1988) show that the effective frictional coupling that generates and dissipates fluatuating rotational energy is distinctly different in the two end-member cases. In particular, the coupling decreases with increasing ratio of relative tangential to normal velocity at impact; or, as collisions become more glancing, the particles become effectively more frictionless. Thus glancing collisions can create and dissipate fluctuating rotational energy when the relative tangential velocity at impact is low, but have little effect on the fluctuating rotations at high relative tangential velocities. As a result, the

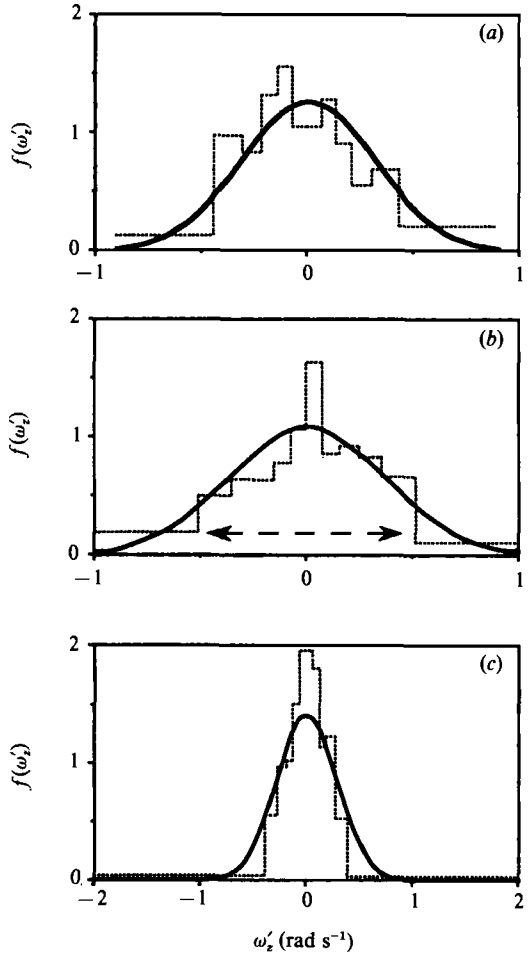

FIGURE 15. Distributions of the in-plane fluctuation rotations ----, ω_z'. ——, Maxwellian, T_{rz}. (*a*) $n = 158$, $y = 0.078$ m. The distributions of ω_z' are approximately Maxwellian in both flows at distances greater than a few particle diameters above the bed. (*b*) $n = 157$, $y = 0.006$ m. In the bin nearest the bed in the disperse flow, the distribution of ω_z' has approximately twice as many particles in the negative tail as in the positive one, a statistically significant difference. The asymmetry is produced by the large number of particle–bed collisions, which produce mostly large negative rotations relative to the number of particle–particle collisions, which produce rotations having both positive and negative sign. (*c*) $n = 501$, $y = 0.018$ m. In the dense flow no asymmetry in ω_z' is evident in the near-bed bins, but the distributions are deficient in particles having medium-magnitude rotations, similar to the behaviour observed for ω_x' and ω_y' (figure 14*a*, *b*).

frequency of high- and low-magnitude fluctuating rotations increases with the frequency of glancing collisions, with a corresponding decrease in the frequency of medium-magnitude fluctuations.

3.2.4. *Rotational temperatures*

For general three-dimensional flows, the rotational temperature T_r can be defined as

$$T_r \equiv \frac{I}{m}(\langle\omega_x'^2\rangle + \langle\omega_y'^2\rangle + \langle\omega_z'^2\rangle), \tag{25}$$

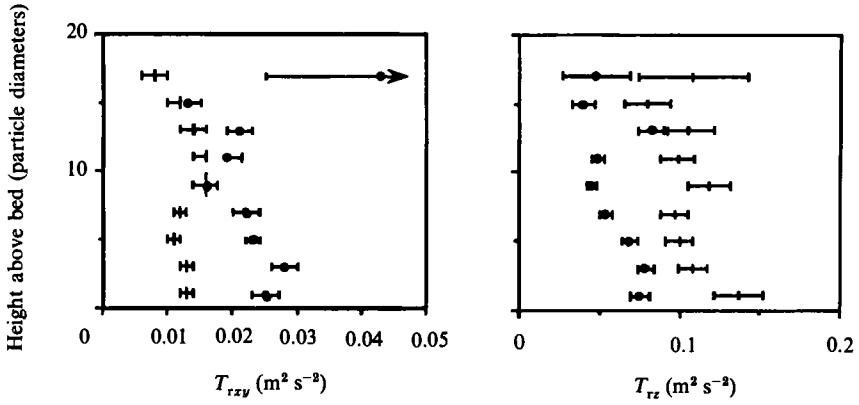

FIGURE 16. (*a*) T_{rxy} is roughly independent of height in both flows. ●, 2230 particles s^{-1}; +, 1280 particles s^{-1}. (*b*) T_{rz} is approximately independent of height in the disperse flow, with the exception of the near-bed datum; it decreases slowly with height in the dense flow, again excepting the near-bed datum.

where I is the moment of inertia of a solid sphere, and m is the mass of a sphere. Here the usual factor of $\frac{1}{3}$ from the kinetic theory of gases (e.g. Dahler & Theodosopulu 1975) has been omitted to emphasize that the energy will not, in general, be equipartitioned between the three rotational modes; thus T_r is a measure of the total rotational fluctuation energy of the flow. In the quasi-two-dimensional experiments it is convenient to define and work with two other rotational temperatures:

$$T_{rxy} \equiv \frac{I}{2m}(\langle\omega_x'^2\rangle + \langle\omega_y'^2\rangle), \tag{26}$$

$$T_{rz} \equiv \frac{I}{m}\langle\omega_z'^2\rangle. \tag{27}$$

T_{rxy} (figure 16*a*) is a measure of the fluctuating rotational kinetic energy arising from experimental deviations from ideal two-dimensionality; T_{rz} (figure 16*b*) is the corresponding measure for the in-plane quantity.

T_{rxy} is approximately independent of height above the bed in both flows. It is small compared to T_{rz} in the disperse flow, which thus closely approximates the two-dimensional ideal; it is a more significant fraction of T_{rz} in the dense flow (figure 17*a*). The behaviour of T_{rz} (figure 16*b*) in the disperse flow might be reasonably approximated as being independent of height, with the exception of the near-bed datum; in the dense flow it decreases with height, again excepting the near-bed datum.

The rotational and translational temperatures for each flow exhibit the same qualitative behaviour, suggesting that the ratio of T_{rz} to $2T_t$ (figure 17*b*) may be roughly constant, but clearly not equipartitioned, in which case $T_{rz}/2T_t = \frac{1}{3}$.

3.2.5. *Stresses*

The kinetic contribution to the stress tensor

$$\boldsymbol{p}_k = \rho\begin{pmatrix}\langle u'^2\rangle & \langle u'v'\rangle \\ \langle u'v'\rangle & \langle v'^2\rangle\end{pmatrix} \tag{28}$$

is simply calculated from the experimental data. However, the relatively large

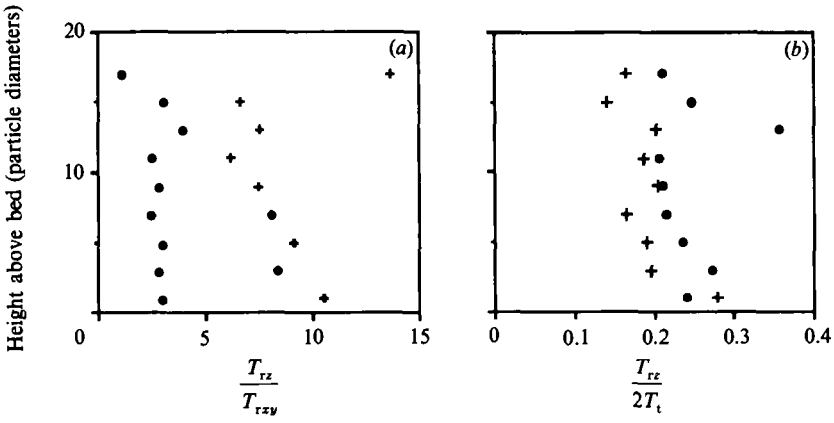

FIGURE 17. (*a*) The ratio of T_{rz} to T_{rxy} is relatively large in the disperse flow, which thus approximates a two-dimensional flow; the same ratio is significantly smaller in the dense flow. ●, 2230 particles s^{-1}; +, 1280 particles s^{-1}. (*b*) Although the ratio of T_{rz} to $2T_t$ is approximately constant in both flows, energy is not equipartitioned between the rotational and translational modes.

uncertainties associated with the fluctuating quantities preclude much useful analysis beyond confirmation that the stress tensor in the dense and disperse flows is indeed dominated by the collisional and kinetic contributions, respectively.

Assuming the flows are steady and uniform, the total normal and shear stresses exerted on planes parallel to the bed are found by integrating the density profile down from the free surface. In the dense flow, the ratio of p_{kyy} to the total normal stress ranged from about 0.35 in the bin nearest the bed to about 0.45 at a height 11 particle diameters above the bed; the ratio increased rapidly with further increase in distance from the bed. In the disperse flow, the minimum ratio of about 0.5 occurred in the bin nearest the bed.

4. Theoretical implications

Although the two-dimensional results presented herein do not apply directly to three-dimensional flows, they nevertheless have broad theoretical implications, because the experimental design preserves the essential physics of the interactions between particles in flows of granular material in which the effects of any interstitial fluid are negligible. The following sections discuss these implications for collisional flows, with particular emphasis on the assumptions underlying kinetic theories of granular flow.

4.1. *The continuum hypothesis*

Theories of granular flow formulate the relations between field variables in terms of partial differential equations. In such theories, the field variables, for example, the bulk density and mean velocity, are assumed to vary continuously in space. In reality, of course, particles in a granular flow are separated by empty space, and thus a continuum formulation implicitly requires averaging particle properties in space and time. The critical question is whether the appropriate averaging can be accomplished. The averaging volume must simultaneously satisfy two criteria: it must contain enough particles that the variables of interest are statistically meaningful (Savage & Lun 1988, pp. 330–332), yet be sufficiently small that changes in the variables across it are negligible. In addition, the averaging time must be

sufficiently short that temporal changes in the variables during the measurement are negligible.

In the flows studied, the averaging time was approximately 2 s, and the averaging area was 2 particle diameters high by 14 diameters long. Beyond the crude assessment of flow steadiness presented in §3, the experiments cannot address whether the averaging-time criteria are satisfied. It seems likely, however, that the criteria will be difficult to satisfy in many time-dependent problems of practical interest, for example, explosion-generated shock waves in granular media.

The experiments suggest that the averaging-area criteria are not satisfied near flow boundaries, because large variations there in such quantities as the mean downstream velocity (cf. figure 8) and the z-component of the mean rotation (cf. figure 10) occur over distances of just two particle diameters. One particle diameter above the bed in the disperse flow, for example, the ratio of $2\sigma(\mathrm{d}u/\mathrm{d}y)$ (the change in velocity over the bin height) to the density-weighted mean downstream velocity was nearly 0.25, and the ratio of $2\sigma(\mathrm{d}\bar{\omega}_z/\mathrm{d}y)$ to the density-weighted mean rotation $\bar{\omega}_z$ was almost 2. On the other hand, at points more than two particle diameters from the boundaries, these ratios had typical values of 0.1 and less. Thus it seems plausible that the averaging-area criteria, and, in turn, the continuum hypothesis, are satisfied in all but a small, albeit important, volume of the nearly steady flows studied. This is not to say, however, that a kinetic-theory-based continuum approach can be developed, because other criteria must be met as well.

4.2. *Collisional grain flows*

The experiments provide a stringent test of many of the assumptions made in deriving kinetic theories for collisional grain flow. Such theories require a complete description of the statistics of particle collisions, which in turn requires both knowledge of the distribution function $f^{(1)}$ and a collision model to describe the outcome of collisions between particles. Finally, the appropriate boundary conditions must be specified.

4.2.1. *Distribution functions*

The distribution function $f^{(1)}$ was approximately Maxwellian for both the translational and rotational velocities in the collisional flows studied, except within a few particle diameters of flow boundaries. There is some theoretical evidence that mean-flow properties are fairly insensitive to the exact form of the velocity-distribution function. Pasquarell & Babic (1988) showed that taking the fluctuation velocities of all particles equal to the r.m.s. fluctuation velocity in a small-gradient, frictionless-particle theory changed the numerical coefficients in the constitutive relations by less than 20% from their values predicted by theories using Maxwellian distributions. The use of such simple distribution functions considerably reduces the mathematical complexity of kinetic theories, and thus may provide a much-needed means of extending them to include particle rotations and realistic boundary conditions.

Finally, the assumption of molecular chaos, or statistical independence of the particle velocities, is implicit in the formulation of the particle-pair velocity distribution function as the product of two single-particle velocity distribution functions. Although the radial distribution function g can be obtained from the experimental data, small sample sizes and concomitant large uncertainties prevent useful quantitative analysis of flow structure. However, structural features observed in dense collisional flows including development of layers of particles and coherent,

roughly equant groups of particles (Drake & Shreve 1986; Drake 1990), and computer simulations indicating strong collisional anisotropy (Campbell & Brennen 1985) indicate that further studies to address the molecular chaos assumption are necessary.

4.2.2. *Collision models*

The illuminating benefits of analytical results from kinetic theories justify the use of simple collision models. Considerable care must be exercised, however, in testing and applying theories to ensure that the models reasonably approximate the true behaviour of colliding particles. In the present experiments, for example, the normal coefficient of restitution ϵ is constant over the experimental range of relative impact velocities. However, it is a strongly decreasing function of the impact velocity for velocities greater than roughly 5 m s^{-1} (the onset of noticeable plastic deformation). Because the tangential coefficient of restitution β is a complex function of the collision geometry and velocities, the normal practice of choosing β = constant may incorrectly describe the behaviour of colliding particles, and in turn, the flow phenomena of interest. The particular choice of constant β to use in theoretical studies, in the absence of a better measure of the transfer of rotational momentum between colliding particles, might best be determined *a posteriori* by an analysis of the sensitivity of the results to β.

Typical 'real' particles are neither identical, geometrically regular, nor homogeneous, and thus the use of theoretically tractable collision models will require an as-yet-unspecified scheme for determining such 'constants' as ϵ and β. Fortunately, it seems likely that many flows can be treated in the context of the simple collision models, provided that the particles are similar in size and material properties (e.g. desert dune sand). Because asperities on the surfaces of contacting sand grains can interlock, $\beta = 0$ (zero post-collision relative tangential surface velocity) is a good assumption, provided the relative velocities are not so high as to break the asperities. Although no such clear-cut argument can be made for constant ϵ, a characteristic feature of theories permitting ϵ to take arbitrary values is that the flow behaviour depends only weakly on the exact value when it is not near 1. Table-top experiments suggest that ϵ for natural sand grains ranges between 0.1 and 0.5, and thus the simple collision models may actually provide better results for flows of rough, nominally uniform size particles than for relatively smooth laboratory particles.

4.2.3. *Boundary conditions*

Significant slip occurs at the fixed bed in these collisional flows despite the considerable roughness of the fixed bed. The energy contained in particle rotations is a significant fraction of the total kinetic energy and should be accounted for in future theories for boundary conditions at solid surfaces. Quantitative evaluation of boundary conditions at a diffuse free surface will typically require consideration of air-drag effects; the present experimental results are in qualitative agreement with the theory of Johnson *et al.* (1990).

5. Discussion

In molecular systems, flow lengthscales are typically many orders of magnitude larger than a molecular diameter. This clear-cut distinction between microscopic and macroscopic scales does not generally hold for granular systems. Thus, because the

particles and their spacing are much larger compared to the scale of the flows compared to ordinary gases, deducing such bulk properties as mean velocity or granular temperature requires analysis of observations on many individual particles. Clearly, some experimental compromise between theoretical ideality and physical reality is necessary to acquire particle-scale information. Limitations imposed by existing technologies and the physical properties of experimental materials constrain the spatial and temporal resolutions of particle-by-particle measurements and the volume of parameter space that can reasonably be explored by physical experiment. This paper concludes with a discussion of these issues and their implications for future microstructural studies of granular materials.

5.1. *Resolution limitations*

A balance must be struck between resolving particle-scale details in time and space, and satisfying the statistical demands of continuum theories. Resolving details implies minimizing both the number of particles and time between observations, while statistical reliability implies maximizing the number of particles observed and total time of observation.

Spatial resolution is limited by the intrinsic resolution of the recording media. The linear number density of particles that can be resolved on a photographic image must be less than the linear number density of image pixels. Allowing only 20 pixels per particle diameter, a measurement area roughly 50 by 35 particles on a side can be recorded on a 10.5 mm by 7.6 mm image (standard 16 mm format), assuming a maximum resolution of roughly 100 pixels mm^{-1}. Analysis of such images may provide mean velocity and bulk density profiles; but greater spatial resolution is typically necessary to address many theoretical and practical issues. Particle rotation measurements, for example, require resolving dots much smaller than a particle diameter.

The most important implication here concerns studies of the transition between collisional regions of flow, in which the binary–collision hypothesis is satisfied, and frictional regions, in which momentum transfer between particles is predominantly effected by persistent frictional interactions. In the transition region free paths become vanishingly small, and the necessary spatial resolution to resolve details of particle trajectories limits the linear dimensions of the observation volume to the order of a few particle diameters. In such cases, ancillary coarse-grained observations must be obtained simultaneously to provide a context for particle-scale information. In the present study the minimum mean free path was about 20% of a particle diameter and the field of view measured approximately 19 by 14 particle diameters.

Four characteristic times arise in considering temporal resolution requirements: (i) the total time of observation, (ii) the sampling interval, which is distinct from (iii) the time between successive photographic images (i.e. reciprocal of the filming rate), and (iv) the image duration, over which time each image integrates the arrival of photons. The total observation time must be sufficiently long that statistical uncertainties in measured flow quantities are acceptable. The total time is typically divided into sampling intervals to obtain ensembles of particle velocities and rotations. Minimizing the sampling interval (subject to the requirement that measurements within each interval are independent, cf. Appendix C) maximizes the total number of observations. Data storage capacity limits the total observation time to at most a few tens of seconds, and more typically several seconds for relatively rapid, collisional flows. Tests of flow steadiness and studies of certain time-dependent problems (e.g. earthquake-induced flow initiation) may necessitate

repetition of experiments to generate statistically valid ensembles, often a difficult proposition due to the sensitivity of flows to initial conditions.

The maximum time between successive images is directly proportional to the mean free path, and inversely proportional to the root-mean-square particle speed. Unambiguous determination of particle velocities and rotations requires particle identification in a minimum of three successive images between collisions, assuming a suitable criterion for an acceptable number of spurious measurements. Image duration is necessarily less than the time between images, and can typically be adjusted to minimize image blur without difficulty. In the present study, 100 ft of 16 mm film (4000 frames) was exposed at a nominal rate of 1440 frames s^{-1} (60 times the normal projection rate); the nominal image duration was 1/3600 s.

5.2. *Flow scale and limitations imposed by material properties*

The most important physical limitations include the overall flow scale and material properties of the experimental particles. The chute length for studies of nominally steady, uniform inclined plane flows should be many tens of flow depths. In turn, efforts to satisfy a continuum hypothesis suggest depths of at least tens of particle diameters. Clearly, use of smaller particles can reduce the overall scale of the flow, but the extraneous influence of air drag increases strongly with decreasing particle size. Furthermore, collisional properties of small particles are highly sensitive to details of the particle-surface geometry (cf. Appendix B) and other surface-related phenomena, most notably electrostatic effects. Limitations on material properties largely prevent physical experiments to test the sensitivity of theoretical predictions, for example, varying ϵ while holding other flow parameters constant. For similar reasons, even qualitative extrapolation of experimental results to different scales – a matter of great practical importance – is fraught with difficulty.

Finally, changes in material properties of experimental particles during the course of experiments may be important; for example, Savage & Sayed (1984, p. 415) observed that the initially smooth, polished surface of glass spheres used in shear-cell tests evolved into a rough, frosted surface during the course of an experiment. In these cases it seems likely that a simple theoretical model describing particle interactions does not apply.

The experiments indicate that development, refinement and extension of continuum models in general and kinetic-theory-based ones in particular will present considerable challenges to theoreticians and experimentalists. On one hand, it remains to be seen just how far such requirements as the continuum and binary-collision hypotheses can be relaxed before theoretical models break down. Computer simulations (e.g. Walton & Braun 1986*a*, *b*) indicate that even the simple kinetic theories are surprisingly robust, despite their apparent shortcomings. On the other hand, physical experiments are often unable to address directly some of the most important of these issues. Properly designed physical experiments are, however, the critical link between computer simulations and theory. They focus attention on particular features critical to testing computer simulations, which in turn offer the detailed particle-scale information needed to test theories.

I thank R. L. Shreve, P. K. Haff, O. R. Walton and M. W. Richman for valuable discussions. This research was supported in part by the National Science Foundation, grants EAR82-12537 and EAR85-04811, the Institute of Geophysics and Planetary Physics at Lawrence Livermore National Laboratory and the University of California.

Appendix A. Material properties of cellulose acetate spheres

Diameter σ	5.99 ± 0.003 mm	Micrometer measurement
Mass m	0.1481 ± 0.002 g	Direct measurement
Density ρ	1.319 g cm^{-3}	Calculated from σ and m
Poisson's ratio ν	0.28	Free-oscillation method (estimate)†
Young's modulus E	3.2 ± 10^{10} dynes cm^{-2}	Free-oscillation method (estimate)†
Shear modulus G	1.3×10^{10} dynes cm^{-2}	Calculated from E and ν
Strength Y	3.3×10^{8} dynes cm^{-2}	Eastman Bulletin MB-34C
Hardness H	9.3×10^{8} dynes cm^{-2}	Calculated from $1.1Y = 0.39H$‡
Friction coefficient μ	0.41 ± 0.02	Slow slider measurement‖ (particle/particle)
Friction coefficient μ_g	0.21 ± 0.07	Kinematic sliding measurement (particle/glass)

† Free-oscillation method (e.g. Soga & Anderson 1967) has not been reliably tested for plastics.
‡ Johnson (1985).
‖ U. Tüzün (private communication, 1987).

Appendix B. Measurement of the normal coefficient of restitution ϵ

The pre- and post-collision particle velocities and rotations were determined from film measurements of 269 binary collisions between 6 mm diameter cellulose acetate spheres in the glass-walled chute. Over the relatively narrow range of impact velocities in the present experiments ϵ is approximately constant (figure 18). Because ϵ is the ratio of two velocities, each with experimental error (see Appendix C), a two-error regression line was fit to the data using the method of York (in Brooks, Hart & Wendt 1972). The slope of the regression line is $\epsilon = 0.84 \pm 0.01$ ($\pm$ indicates one standard deviation) and the y intercept is 0.01 ± 0.03.

Appendix C. Data acquisition, analysis and errors

This Appendix describes the digitizing procedure, the errors in determining centre and dot locations and the resulting errors in particle velocities and spins. Although present image-processing technologies can efficiently assimilate the enormous amount of data on the films, these capabilities were unavailable at the time. Thus, quantitative information was extracted from films by projecting the image onto a computer-driven, wall-mounted digitizing tablet and manually locating the centres of particles and dots with a bulls-eye cursor. Further details of the data-acquisition procedures are found in Drake (1988).

To determine profiles of the various velocities and spins, measurements of each particle visible in the film frame were made at regular intervals along the film. The sampling interval was chosen to ensure no correlation between particle velocities and spins between measurements. The error in locating a particle centre was determined by repeatedly digitizing two fiducial marks and a single particle centre on one film frame. The components of the deviations of each measured centre from the mean centre were independent and normally distributed with standard deviation $\sigma = 0.022$ particle diameters (0.132 mm). The distribution of the deviation components does not vary significantly in different parts of the film image or between projectionists.

Errors in velocity arise from differencing two centre locations and dividing by the time δt between measurements. The error in determining δt is negligible relative to

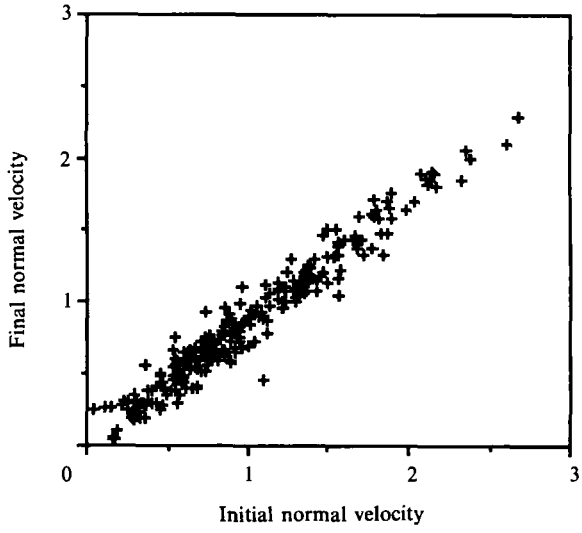

FIGURE 18. Analysis of 269 binary collisions spanning the experimental range of impact velocities gives a normal coefficient of restitution $\epsilon = 0.84 \pm 0.01$, determined from a two-error regression line (not shown) fit to the data using the method of York (in Brooks *et al.* 1972). The slope of the regression line is ϵ and the y-intercept is 0.01 ± 0.03.

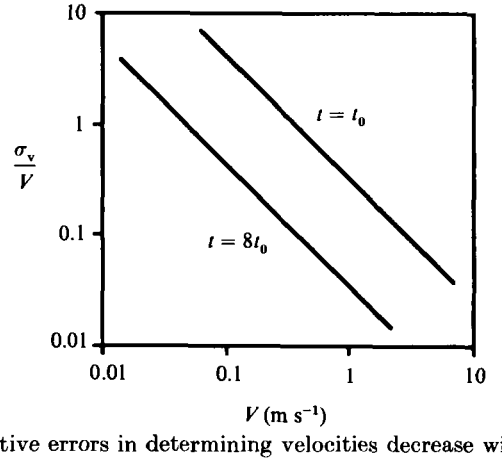

FIGURE 19. Relative errors in determining velocities decrease with increasing velocity.

location errors. Errors in the locations X_{1i} and X_{2i} were normally distributed with zero mean and variance σ^2, so the velocity V_i is also normally distributed with parameters

$$\overline{V}_i = D_i/\delta t, \quad \text{Var}\, V_i = \sigma_v^2 = 2\sigma^2/\delta t^2, \tag{C 1}$$

where D_i is the expected value of $X_{1i} - X_{2i}$. The typical relative error in velocity measurements

$$\frac{\sigma_v}{V_i} = \frac{\sqrt{2}\sigma}{V_i t} = \frac{\sqrt{2}\sigma}{D_i} \tag{C 2}$$

is inversely proportional to the displacement (figure 19).

Errors in spin arise primarily from errors in locating the particle centres. A particle centre and two dots were digitized repeatedly, and angular displacement vectors describing the rotation from the mean of the measured dot positions to each pair of

dots were computed. The root-mean-square angular displacement is 0.11 radians, which corresponds to a typical r.m.s. spin error of 21 radians s^{-1}, assuming 8 film frames between measurements and a filming rate of 1500 frames s^{-1}.

REFERENCES

AHN, H. 1989 Experimental and analytical investigations of granular materials: shear flow and convective heat transfer. PhD dissertation, California Institute of Technology, Division of Engineering and Applied Science Report E200.28, Pasadena, California, USA.

ARAKI, S. & TREMAINE, S. 1986 The dynamics of dense particle disks. *Icarus* **65**, 83–109.

BATCHELOR, G. K. 1967 *An Introduction to Fluid Dynamics*. Cambridge University Press.

BROOKS, C., HART, S. R. & WENDT, I. 1972 Realistic use of two-error regression treatments as applied to rubidium–strontium data. *Rev. Geophys. Space Phys.* **10**, 551–577.

CAMPBELL, C. S. & BRENNEN, C. E. 1985 Computer simulation of granular shear flows. *J. Fluid Mech.* **151**, 167–188.

CARTWRIGHT, P., SINGH, S. & BAILEY, A. G. 1985 Electrostatic charging characteristics of polyethylene powder during pneumatic conveying. *IEEE Trans. Indust. Applic.* **11**, 541–546.

DAHLER, J. S. & THEODOSOPULU, M. 1975 The kinetic theory of dense polyatomic fluids. *Adv. Chem. Phys.* **31**, 155–229.

DRAKE, T. G. 1988 Experimental flows of granular material. PhD dissertation, University of California, Los Angeles, California, USA.

DRAKE, T. G. 1990 Structural features in granular flows. *J. Geophys. Res.* **95**, 8681–8696.

DRAKE, T. G. & SHREVE, R. L. 1986 High-speed motion pictures of nearly steady, uniform, two-dimensional inertial flows of granular material. *J. Rheol.* **30**, 981–993.

GUTT, G. 1987 A continuum theory of granular flow including spin. *Caltech Brown Bag series*, BB-59.

GUTT, G. & HAFF, P. K. 1988 Boundary conditions on continuum theories of granular flow. *Caltech Brown Bag series*, BB-70.

HAFF, P. K. 1983 Grain flow as a fluid-mechanical phenomenon. *J. Fluid Mech.* **134**, 401–430.

JENKINS, J. T. & RICHMAN, M. W. 1985*a* Grad's 13-moment system for a dense gas of inelastic spheres. *Arch. Rat. Mech. Anal.* **87**, 355–377.

JENKINS, J. T. & RICHMAN, M. W. 1985*b* Kinetic theory for plane flows of a dense gas of identical, rough, inelastic, circular disks. *Phys. Fluids* **28**, 3485–3494.

JENKINS, J. T. & RICHMAN, M. W. 1986 Boundary conditions for plane flows of smooth, nearly elastic, circular disks. *J. Fluid Mech.* **171**, 53–69.

JENKINS, J. T. & RICHMAN, M. W. 1988 Plane simple shear of smooth, inelastic, circular disks: the anisotropy of the second moment in the dilute and dense limits. *J. Fluid Mech.* **192**, 313–328.

JENKINS, J. T. & SAVAGE, S. B. 1983 A theory for the rapid flow of identical, smooth, nearly elastic, spherical particles. *J. Fluid Mech.* **130**, 187–202.

JOHNSON, P. C., NOTT, P. & JACKSON, R. 1990 Frictional–collisional equations of motion for particulate flows and their application to chutes. *J. Fluid Mech.* **210**, 501–535.

JOHNSON, K. L. 1985 *Contact Mechanics*. Cambridge University Press.

LUN, C. K. K. & SAVAGE, S. B. 1987 A simple kinetic theory for granular flow of rough, inelastic, spherical particles. *J. Appl. Mech.* **54**, 47–53.

LUN, C. K. K., SAVAGE, S. B., JEFFERY, D. J. & CHEPURNIY, N. 1984 Kinetic theories for granular flow – inelastic particles in a Couette flow and slightly inelastic particles in a general flow field. *J. Fluid Mech.* **140**, 223–256.

MINDLIN, R. D. & DERESIEWICZ, H. 1953 Elastic spheres under varying oblique forces. *J. Appl. Mech.* **21**, 237–244.

PASQUARELL, G. C. & BABIC, M. 1988 On the form of the velocity distribution for collisional constitutive relations. In *Abstracts for the Seventh Engineering Mechanics Specialty Conference*, p. 12. ASCE, 23–25 May 1988, Blacksburg, Virginia.

RICHMAN, M. W. & CHOU, C. S. 1989 Boundary effects on granular shear flows. *Z. angew Math. Phys.*, in press.

SAVAGE, S. B. 1982 Granular flows down rough inclines – review and extension. In *Proc. US–Japan seminar on new models and constitutive relations in the mechanics of granular materials* (ed. J. T. Jenkins & M. Satake), pp. 232–281. Elsevier.

SAVAGE, S. B. 1983 Granular flows at high shear rates. In *Theory of Dispersed Multiphase Flow* (ed. R. E. Meyer), pp. 339–358. Academic Press.

SAVAGE, S. B. 1984 The mechanics of rapid granular flows. In *Advances in Applied Mechanics*, vol. 24 (ed. J. Hutchinson & T. Y. Wu), pp. 289–366. Academic Press.

SAVAGE, S. B. & LUN, C. K. K. 1988 Particle size segregation in inclined chute flow of dry cohesionless granular solids. *J. Fluid Mech.* **189**, 311–335.

SAVAGE, S. B., NEDDERMAN, R. M., TÜZÜN, U. & HOULSBY, G. T. 1982 The flow of granular materials, 3. Rapid shear flows. *Chem. Engng Sci.* **38**, 189–195.

SAVAGE, S. B. & SAYED, M. 1984 Stresses developed by dry cohesionless granular materials sheared in an annular shear cell. *J. Fluid Mech.* **142**, 391–430.

SOGA, N. & ANDERSON, O. L. 1967 Elastic properties of tektites measured by resonant sphere technique. *J. Geophys. Res.* **72**, 1733–1739.

STRINGHAM, G. E., SIMONS, D. B. & GUY, H. P. 1969 The behavior of large particles falling in quiescent liquids. *US Geol. Survey Professional Paper* 562-C.

WALTON, O. 1983 Particle-dynamics calculations of shear flow. In *Proc. US–Japan seminar on new models and constitutive relations in the mechanics of granular materials* (ed. J. T. Jenkins & M. Satake), pp. 327–338. Elsevier.

WALTON, O. R. & BRAUN, R. L. 1986*a* Viscosity, granular-temperature and stress calculations for shearing assemblies of inelastic, frictional disks. *J. Rheol.* **30**, 949–980.

WALTON, O. R. & BRAUN, R. L. 1986*b* Stress calculations for assemblies of inelastic spheres in uniform shear. *Acta Mech.* **63**, 45–60.

WALTON, O. R. & DRAKE, T. G. 1988 Granular flow in a two-dimensional channel: a comparison of measurements and numerical simulations. In *Abstracts for the Seventh Engineering Mechanics Specialty Conference*, p. 4. ASCE, 23–25 May 1988, Blacksburg, Virginia.

WERNER, B. T. & HAFF, P. K. 1986 A simulation study of the low energy ejecta resulting from single impacts in eolian saltation. In *Advancements in Aerodynamics, Fluid Mechanics and Hydraulics* (ed. R. E. A. Arndt), pp. 337–345. ASCE.